Vision-driven Autocharacterization of Perovskite Semiconductors

Alexander E. Siemenn[1,*], **Eunice Aissi**[1,*], Fang Sheng[1], Armi Tiihonen[2], Hamide Kavak[3], Basita Das[1], and Tonio Buonassisi[1]

[1]Department of Mechanical Engineering
Massachusetts Institute of Technology
Cambridge, MA 02193, USA
[*]{asiemenn@mit.edu,
eunicea@mit.edu}

[2]Department of Applied Physics
Aalto University
P.O. Box 11100, Aalto, Finland

[3]Department of Physics
Cukurova University
Adana, 01330, Turkey

Abstract

In materials research, the task of characterizing hundreds of different materials traditionally requires equally many human hours spent measuring samples one by one. We demonstrate that with the integration of computer vision into this material research workflow, many of these tasks can be automated, significantly accelerating the throughput of the workflow for scientists. We present a framework that uses vision to address specific pain points in the characterization of perovskite semiconductors, a group of materials with the potential to form new types of solar cells. With this approach, we automate the measurement and computation of chemical and optoelectronic properties of perovskites. Our framework proposes the following four key contributions: (i) a computer vision tool for scalable segmentation to arbitrarily many material samples, (ii) a tool to extract the chemical composition of all material samples, (iii) an algorithm capable of automatically computing band gap across arbitrarily many unique samples using vision-segmented hyperspectral reflectance data, and (iv) automating the stability measurement of multi-hour perovskite degradation experiments with vision for spatially non-uniform samples. We demonstrate the key contributions of the proposed framework on eighty samples of unique composition from the formamidinium-methylammonium lead tri-iodide perovskite system and validate the accuracy of each method using human evaluation and X-ray diffraction.

1. Introduction

Computer vision approaches have the potential to accelerate the characterization process of novel alloys that are in demand for applications ranging from solar to structural materials [14, 6]. Innovating new alloys is challenging, in part because the composition space is vast, requiring numerous cycles of synthesis and characterization [22, 23]. Furthermore, numerous cycles of learning are time- and cost-prohibitive to perform manually. These pain points in the domain of material synthesis can be targeted via laboratory automation. Siemenn *et al.* [21] and MacLeod *et al.* [10] recently demonstrated autonomous hardware systems capable of significantly accelerating the cycles of learning for material synthesis. However, to realistically accelerate the process of novel material discovery, one has to match the high-throughput synthesis loop with equally as fast characterization. The scalability of the pipeline is not only a matter of accelerating the characterization of individual samples but depends also on the breadth of the pipeline, *e.g.*, the number of samples required to be characterized. Computer vision has the capacity to scale to arbitrarily many samples without significantly increasing the duration of each characterization step [5, 9, 17].

Thus, in this contribution, we propose an automated materials characterization pipeline that is fully based on computer vision. We demonstrate this automated vision-based characterization loop using (i) a computer vision tool for scalable segmentation to arbitrarily many material samples, (ii) a tool to extract the chemical composition of all material samples, (iii) an algorithm capable of automatically computing band gap across arbitrarily many unique samples using vision-segmented hyperspectral reflectance data, and (iv) automating the stability measurement of multi-hour perovskite degradation experiments with vision for spatially non-uniform samples. The accuracy of each developed method is benchmarked against human evaluation and X-ray diffraction.

1.1. Related Work

Increasing levels of laboratory automation, machine learning, and other algorithmic approaches enable the development of accelerated, integrated approaches to investigate novel materials [14, 10, 6, 19]. Generally, there is high interest in many use cases for parsing through large image data sets using computer vision, for example, Garnot *et al.* [5] developed algorithms for time series analysis of satel-

[*] Corresponding authors; contributed equally.

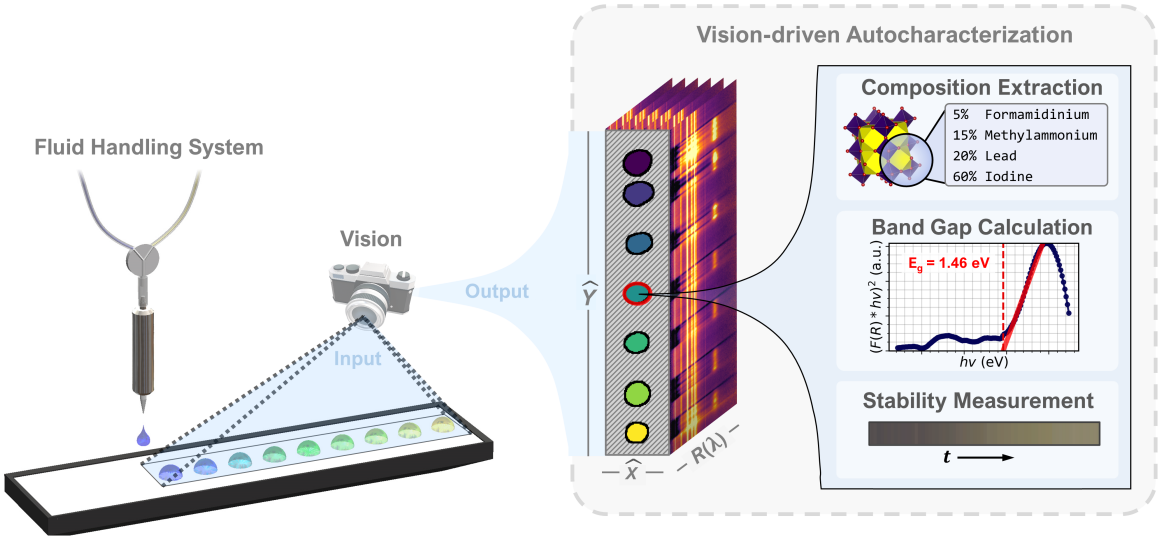

Figure 1: The workflow for autocharacterization of perovskite semiconductors using computer vision. From left to right: A fluid handling system mixes and deposits each unique semiconductor material onto a plate. The vision system captures images in RGB and hyperspectral channels (wavelengths $\lambda \in [380\text{nm}, 1020\text{nm}]$), then segments the pixels of each material deposit (X, Y, λ) from the background. The (i) compositional information, (ii) direct band gap, and (iii) stability of each unique sample are automatically characterized using the optical data segmented by the vision system.

lite images. Computer vision is gaining traction specifically in rapid morphological material characterization and is increasingly being used to analyze large sets of microscope images [17]. As such, multiple analytical computer vision tools have been developed to access material morphology, often focused on identifying microstructures of materials. For example, Park *et al.* [18] created a semi-automated image segmentation and analysis algorithm to extract the morphology of nano-particles from image data. Likewise, Chowdhury *et al.* [3] utilized computer vision and machine learning to detect dendritic microstructures from a database of solder alloy micrographs. There is also extensive work surrounding materials recognition in non-micrographic images using computer vision [2, 8]. In order to support the growing need for micrographs and other experimental image analysis, advances like those made by Li *et al.* [9], Wang *et al.* [24], and Neshatavar *et al.* [16] on object segmentation and denoising allow for further use cases of computer vision in scientific research.

The development of autocharacterization methods of materials is not novel, however, little literature exists on driving autocharacterization with computer vision to accelerate throughput and increase algorithm scalability to arbitrarily many samples. Escobedo-Morales *et al.* [4] design an automated band gap calculation tool from reflectance data, however, their implementation does not employ automatic vision segmentation, hence, the approach is limited to single sample-by-sample processing. Furthermore, the process of band gap curve fitting using inclination angles developed by Escobedo-Morales *et al.* [4] produces numerical inconsistencies and is removed in our implementation in favor of a simpler and more robust version of RMSE minimization. Keesey & Tiihonen *et al.* [7] develop a procedure of optically extracting a figure of merit to quantify the stability of perovskites but this methodology requires the manual segmentation of samples one by one, which becomes infeasible for a human researcher when the number of samples increases significantly. In this paper, we build from these prior works by demonstrating the performance of three autocharacterization methods that are scalable to arbitrarily many samples using a computer vision-driven approach.

2. Methods

In this paper, we develop four processes for the autocharacterization of perovskites: (i) a hyperspectral vision segmentation process, (ii) an automatic composition extractor, (iii) an automatic band gap computation algorithm, and (iv) an automatic stability measurement method. All the code required for reproducing the autocharacterization results described in this contribution **will be made publicly available in full publication**.

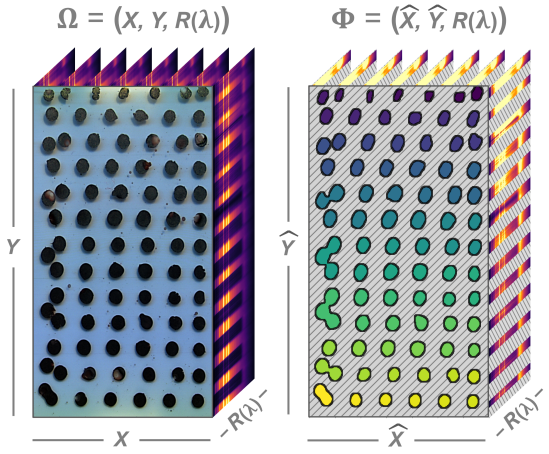

(a) Raw Image (b) Vision-segmented Image

Figure 2: Vision segmentation of hyperspectral datacubes to locate the reflectance pixel values for material deposits only. (a) Raw image that contains reflectance information, R, for all pixels, (X, Y), including the background; (b) vision-segmented image that contains reflectance information for only the target material deposit pixels with a unique feature index assigned to each deposit $(\widehat{X}, \widehat{Y})$. Through the segmentation process described by Algorithm 1, background pixels are removed, illustrated by the gray hatches in (b), such that only the circular material deposit pixels and their corresponding R remain. Furthermore, all material deposit pixels are assigned a unique feature index, illustrated by the purple-to-yellow colormap. Using this segmentation and unique index assignment, the optical data in the R-domain is uniquely mapped onto the deposit it was measured from. This process is equivalent for λ values in both Hyperspectral and RGB regimes.

2.1. Experiments

In this study, we synthesize 80 unique perovskite compositions within the formamidinium-methylammonium lead tri-iodide perovskite system, $FA_{1-x}MA_xPbI_3$. These 80 materials are synthesized using a high-throughput liquid deposition tool, as described in Siemenn *et al.* [21]. In brief, the perovskites are deposited onto an amorphous glass slide by pumping fluid from two sources containing the liquid-based precursors of methylammonium lead iodide ($MAPbI_3$) and formamidinium lead iodide ($FAPbI_3$). The total time to deposit all 80 samples is 16.5 seconds and each pump runs at a rotational velocity that may vary over this total time. Hyperpectral optical data is recorded across the batch of 80 samples as a single image for band gap analysis. The eighty perovskite samples were degraded under 50°C temperature, 35% air humidity, and 0.5 sun illumination (visible only) for 6 hours to assess stability via color change, captured with RGB imaging. The hyperspectral data are acquired with the Resonon, Inc. Pika L camera and the RGB data are acquired with the Thorlabs, Inc. DCC1645C camera.

2.2. Hyperspectral and RGB Vision Segmentation

The common thread across the composition, band gap, and stability autocharacterization processes is the vision segmentation framework. The desired output of the segmentation procedure is the segmented optical data Φ, a set of uniquely indexed optical data for each material deposit:

$$\Phi = (\widehat{X}, \widehat{Y}, R(\lambda)),$$
$$\lambda = \begin{cases} \{a \mid 380 \leq a \leq 1020\}, & \text{if Hyperspectral} \\ \{700, 546, 435\}, & \text{if RGB,} \end{cases} \quad (1)$$

where $(\widehat{X}, \widehat{Y}, R(\lambda))$ is the 3D datacube of segmented and indexed pixels, $(\widehat{X}, \widehat{Y})$, for each material with the corresponding reflectance intensity data, $R(\lambda)$, at the wavelengths λ in nanometers (nm).

Algorithm 1: Vision Segmentation

Input : $(X, Y, R(\lambda))$: All image pixels and reflectance
Θ_{min}: Minimum segmented feature size
Θ_{max}: Maximum segmented feature size

Output : $(\widehat{X}, \widehat{Y}, R(\lambda))$: Segmented pixels and reflectance

Let κ be kernel size
img $\leftarrow (X, Y, R(\lambda))$
img $\leftarrow$ `Crop`(img)
img $\leftarrow$ `Grayscale`(img)
img $\leftarrow$ 255 - img
mask $\leftarrow$ `Binarize`(img)
mask $\leftarrow$ `MorphGradient`(mask, $\kappa = 12$)
mask $\leftarrow$ `Erode`(mask, $\kappa = 3$)
mask $\leftarrow$ `MedianBlur`(mask, $\kappa = 7$)
mask $\leftarrow$ `DistTransform`(mask, $\kappa = 3$)
mask $\leftarrow$ `LabelFeatures`(mask)
$(\widehat{X}, \widehat{Y}) \leftarrow$ `Watershed`(img, mask)
$(\widehat{X}, \widehat{Y}) \leftarrow$ `Dilate`$((\widehat{X}, \widehat{Y}), \kappa = 5)$
$(\widehat{X}, \widehat{Y}) \leftarrow$ `MedianBlur`$((\widehat{X}, \widehat{Y}), \kappa = 7)$
for ϕ in `Feature`$((\widehat{X}, \widehat{Y}))$ **do**
  if `Size`$(\phi) < \Theta_{\text{min}}$ **or** `Size`$(\phi) > \Theta_{\text{max}}$ **then**
    $(\widehat{X}, \widehat{Y})$`.Prune`$(\phi)$
  end
end
bool $\leftarrow$ `Boolean`$((\widehat{X}, \widehat{Y}))$
$(\widehat{X}, \widehat{Y}, R(\lambda)) \leftarrow (X, Y, R(\lambda))$`.Mask`(bool)

Return $(\widehat{X}, \widehat{Y}, R(\lambda))$

The raw image datacube without segmentation is $\Omega = (X, Y, R(\lambda))$. To obtain Φ, $(X, Y, R(\lambda))$ is passed through

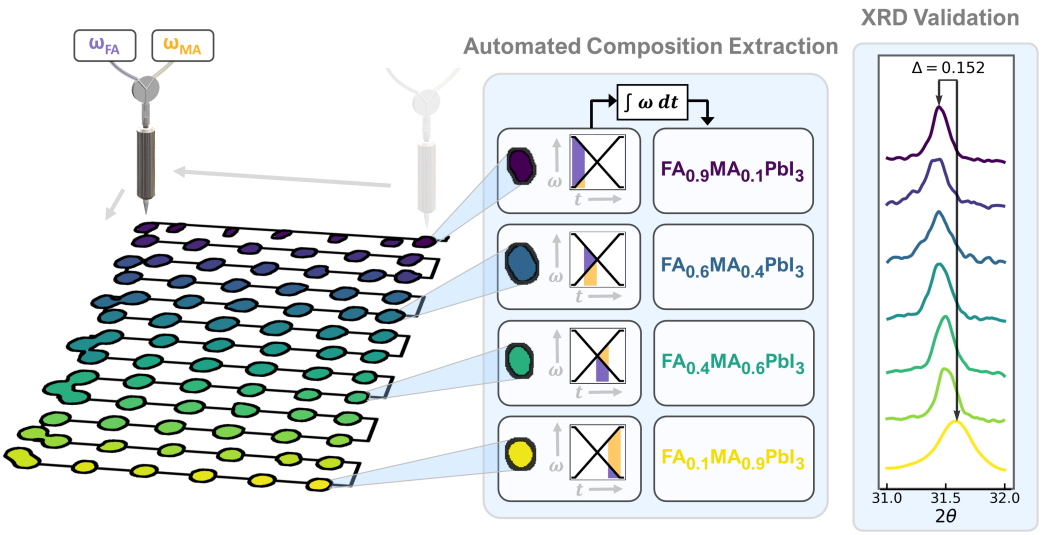

Figure 3: Automated extraction of chemical composition from vision-segmented perovskite deposits synthesized using a high-throughput liquid deposition system. From left to right: A liquid handling system rasters along the black path, depositing perovskite semiconductors of varying composition by temporally varying the two pump rotational velocities, ω_{FA} and ω_{MA}; the rotational velocity ω_{FA} governs the proportion of FA in the deposit while the rotational velocity ω_{MA} governs the proportion of MA in the deposit; these time-dependent velocities are obtained directly from the pump microcontrollers and are plotted as the black diagonal lines in the t versus ω subplots; the integrals of the ω's over time for four vision-segmented deposits are shown as the purple and yellow areas beneath the black curves; computing the integral solves for x to estimate the composition $\text{FA}_{1-x}\text{MA}_x\text{PbI}_3$. This method is validated by XRD measurement. The right panel illustrates a peak shift of $+0.152°$ in 2θ from measured deposits with a high expected FA proportion (purple) to measured deposits with high expected MA proportion (yellow), which is the expected result.

several filters to find the edges of each feature and then index the features appropriately. In this study, the input image dimensions are $(900, 600)$ pixels and each feature has an area of roughly 1000 pixels. There are approximately 80 features in the image area but their number and location vary from experiment to experiment. Inputting images or features of different sizes may require tuning the kernel sizes, κ, of the filters.

Algorithm 1 describes this segmentation process of $(X, Y, R(\lambda)) \rightarrow (\widehat{X}, \widehat{Y}, R(\lambda))$. First, the input image is cropped and converted to greyscale, then it is passed through several layers of thresholding and smoothing. By thresholding, eroding, blurring, and then thresholding again, we capture the edges of each feature while removing edge effects. The background is indexed as zeros, hence, all features split by zeros are assigned a unique index using `LabelFeatures`$(\cdot)$ and `Watershed`$(\cdot)$ [13]. Once segmented, the features are smoothed, and any improperly segmented aberrations are pruned with the user-selected hyperparameters Θ_{min}, Θ_{max}. Finally, a boolean mask is created for all pixels encoded with non-zero values to output Φ, where each uniquely indexed material deposit is directly mappable to the $R(\lambda)$ measured for that deposit. Figure 2(a) shows the unprocessed, raw hypercube of perovskite semiconductor reflectance intensity data, R, and Figure 2(b) shows the post-processed, segmented hypercube, output by Algorithm 1.

Generating a clean segmented image mappable to optical reflectance data provides a powerful foundation for further characterization of material properties. In this paper, We use the output Φ to automatically extract compositional, band gap, and stability information from each unique perovskite deposit.

2.3. Automatic Composition Extraction

In the perovskite semiconductor system, the performance metrics of band gap and stability are largely governed by the chemical composition of the material [23, 7]. However, since the 80 samples are synthesized using the high-throughput method described in Section 2.1, the exact composition of each unique deposit (the value of x) is not known *a priori*. Traditionally, X-ray photoelectron spectroscopy (XPS) is used to determine the chemical composition but XPS is a time-consuming process. Here, we extract the compositional information automatically and deterministically from the segmented image by mapping it with the

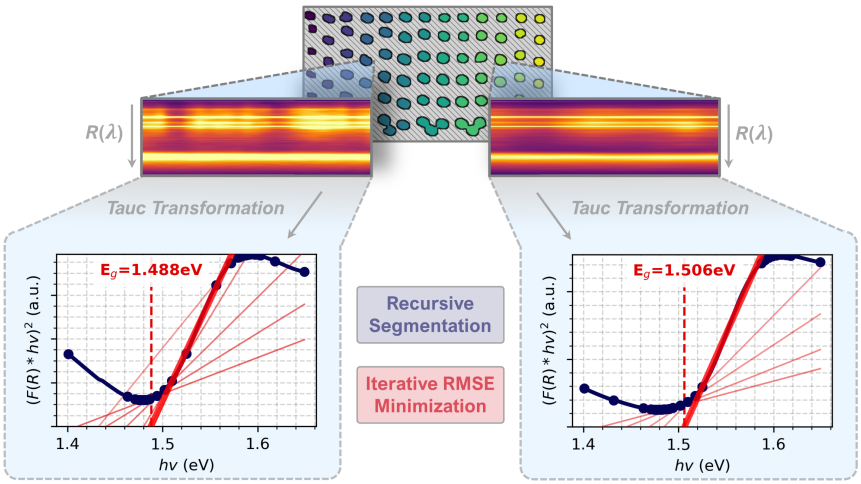

Figure 4: Automatic band gap computation from vision-segmented perovskite deposits. From top to bottom: The reflectance intensities, $R(\lambda), \lambda \in [380\text{nm}, 1020\text{nm}]$, are acquired for each sample from the vision-segmented hypercube, Φ (obtained from a single image of a hyperspectral camera); the Tauc curves are computed from the median reflectance across all wavelengths for each deposit; each Tauc curve is recursively segmented into small line segments and then iteratively fit with linear regression lines; the regression line that minimizes the RMSE with the Tauc curve is illustrated by the thick red line, which computes the band gap, E_g.

synthesis conditions of the liquid deposition tool over space, as shown in Figure 3 and in the following expression:

$$x(\Phi) = \int_{t_a(\Phi)}^{t_b(\Phi)} \frac{\omega_{\text{MA}}(\Phi)}{(\omega_{\text{MA}}(\Phi) + \omega_{\text{FA}}(\Phi))} dt, \qquad (2)$$

where $\omega_{\text{MA}}(t)$ and $\omega_{\text{FA}}(t)$ are the rotational velocities of the MA and FA precursor pumps, respectively, as a function of time t. These time-dependent rotational velocities are acquired directly from the pump microcontrollers and are visualized in the middle panel in Figure 3. The time-dependent coordinates of the fluid deposition system's raster path are acquired directly from the system G-code and are visualized as the black pathway beneath the deposits in the left panel of Figure 3. Hence, the pump velocity timestamps and the raster coordinate timestamps are bi-directionally mappable to each other: $t(X, Y) \leftrightarrow t(\omega_{\text{MA}}, \omega_{\text{FA}})$. Therefore, both the pump velocities, $\omega_{\text{MA, FA}}(\Phi)$, and the integration time, $t_b(\Phi) - t_a(\Phi)$, for each material deposit are obtainable from the vision-segmented data, Φ, and $x(\Phi)$ is computed using Equation 2 to solve $\text{FA}_{1-x}\text{MA}_x\text{PbI}_3$.

2.4. Automatic Band Gap Computation

Computing the band gap of a semiconductor material often requires laborious manual curve fitting to Tauc plots [22] that result in human error and consume time. Current band gap computing software from literature still requires each sample to be processed one by one, which becomes infeasible for large numbers of samples produced by high-throughput synthesis tools. We develop a band gap computation tool that takes in the vision-segmented hyperspectral data, Φ, for each deposited sample and accurately computes each band gap autonomously. This developed process is agnostic to the number of samples and will scale up to higher numbers of samples, accelerating the material characterization process.

Figure 4 illustrates the workflow of the automatic band gap computation procedure. First, the hyperspectral reflectance, $R(\lambda)$, is acquired from the vision segmentation output, Φ, for each sample. The median $R(\lambda)$ for all $(\widehat{X}, \widehat{Y})$ per sample is taken to minimize the influence of outlier pixels and edge effects on the reflectance. Then, reflectance is transformed into a Tauc curve for each sample using the following equation [11]:

$$F(R(\lambda; \widehat{X}, \widehat{Y})) = \left(\frac{620(1 - R(\lambda; \widehat{X}, \widehat{Y}))^2}{\lambda R(\lambda; \widehat{X}, \widehat{Y})} \right)^{\frac{1}{\gamma}}, \qquad (3)$$

where γ is a constant value of $\frac{1}{2}$ or 2 for direct band gap or indirect band gap, respectively. We compute the direct band gap for $\text{FA}_{1-x}\text{MA}_x\text{PbI}_3$ perovskites, hence, $\gamma = \frac{1}{2}$. The transformed Tauc curves are then recursively segmented into linear segments that are split in half until every segment achieves a coefficient of determination of $R^2 \geq 0.990$. As shown in the bottom panels of Figure 4, the dark blue markers along the Tauc curve have a higher density along curved

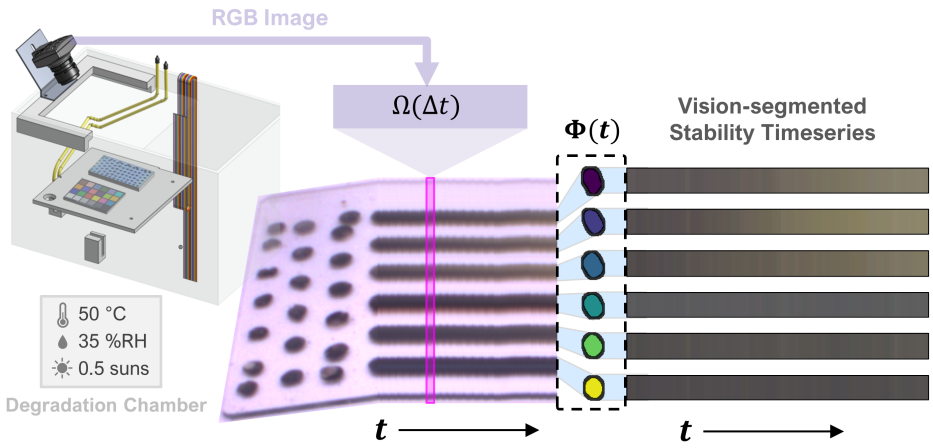

Figure 5: Automatic degradation testing of vision-segmented perovskite deposits. The aging test is started by taking a single image of a reference color chart on the sample holder plate. The chart is swapped with the samples that are continuously degraded under environmental stress for 6 hours and photographed using an RGB camera with 10-second intervals. The segmented color time series is averaged over the pixels in each sample, color calibrated, and analyzed by calculating the instability index from the data.

regions, indicating a higher segmentation rate is required to form straight line segments. Once the recursion is complete, each pair of adjacent line segments is iteratively fit with a linear regression line, as shown by the thin red lines in the bottom panels of Figure 4. The root-mean-square error (RMSE) is computed between each regression line and the Tauc curve within the range of the x-intercept and the Tauc peak location minus one-half of the peak width. Enforcing the RMSE computation within this range was shown to increase fitting accuracy. The band gap, E_g, is the x-intercept point of the regression line that minimizes the RMSE.

2.5. Automatic Stability Measurement

A helpful property in screening potential perovskite crystal structures is their stability under relevant environmental conditions. For example, in solar panels, the lifetime of the perovskite semiconductor under given illumination conditions, humidity levels, and temperature are all deterministic of possible applications. To determine stability, the perovskite semiconductors were subject to an accelerated degradation chamber, and the three-channel RGB approximation of the color change of the sample was recorded as a proxy to sample stability. [7] The chamber, pictured in Figure 5, maintains a uniform temperature, illumination, and humidity level around the samples, and obtains real-time images of the perovskite semiconductors every time step Δt for a duration of time T resulting in $\Omega(\Delta t)$ images. [7] The vision segmentation algorithm described in Algorithm 1 is applied to the first droplet image, Ω, to output the segmented locations and reflectance data, Φ, of each spatially-non uniform sample across the duration of the experiment with a fixed camera position.

In order to use color as a reproducible and repeatable quantitative proxy for degradation, color calibration needs to be applied because the illumination conditions in the aging test chamber may vary over time. At the beginning of the degradation study, an image of a reference color chart (X-Rite Colour Checker Passport; 28 reference color patches), I_R, is taken under the same illumination conditions as the perovskite semiconductor samples. Images at each time step, $\Omega(\Delta t)$, are transformed into L*a*b and subsequently to a stable reference color space (standard observer CIE 1931 2 degrees, standard illuminant D50) by applying a 3D-thin plate spline distortion matrix D [23, 12] defined by I_R and known colors of the reference color chart:

$$D = \begin{bmatrix} V \\ O(4,3) \end{bmatrix} \begin{bmatrix} K & P \\ P^T & O(4,4) \end{bmatrix}^{-1} \tag{4}$$

Here, $O(n,m)$ is an nxm zero matrix, V is a matrix of the color checker reference colors in the stable reference color space, P is a matrix of the color checker RGB colors obtained from I_R, and K is a distortion matrix between the color checker colors in the reference space and in I_R.

Using the color-calibrated images and droplet pixel locations given by Φ, a final array, $R(t;\widehat{X},\widehat{Y})$ of the average color at time t for perovskite semiconductor of composition $FA_{1-x}MA_xPbI_3$ is created. The color of each droplet is measured to determine a stability metric I_c [23]:

$$I_c(\widehat{X},\widehat{Y}) = \sum_{R=\{r,g,b\}} \int_0^T |R(t;\widehat{X},\widehat{Y}) - R(0;\widehat{X},\widehat{Y})|dt \tag{5}$$

Here, the color is averaged over sample pixels and is collected from red (r), green (g), and blue (b) color channels.

3. Results

Combining the three vision-driven autocharacterization processes developed in this paper accelerates the identification of perovskite semiconductors with desirable properties relative to conventional human-evaluated characterization. Using the segmented optical data, Φ, of each sample composition, band gap, and stability are all computed automatically. This combination is a sufficient number of characterizations for a pipeline that initially screens perovskite materials properties, which we demonstrate can be implemented fully via computer vision techniques. In this section, we visualize the characterization results output by each automated process and benchmark them against human evaluation.

Figure 6 shows the band gap and instability index as a function of sample composition computed using autocharacterization. The computed band gap of each composition is shown to have a linearly increasing trend with an increasing proportion of MA. Furthermore, the computed band gap values fall within a range of 1.45eV–1.52eV. This eV range and linearly increasing trend align with the anticipated results from literature as the MA proportion is increased within the $FA_{1-x}MA_xPbI_3$ system, for example, Weber et al. report a linear trend within a range of 1.45eV–1.55eV [25, 22].

The computed instability index of each composition peaks at approximately 25% MA content, indicating more degradation occurs closer to the FA-rich compositions, but not at purely $FAPbI_3$ compositions. Through visual inspection of the degradation results, we manually threshold the instability index at $I_c > 10000$ px ·min to classify samples with high degradation rates, i.e., the samples with MA proportions between 10%–40%. Patterns of high stability in FA-pure perovskites that decrease as MA is added are seen within literature, for example when the samples are degraded under high heat and humidity [23], however, the trends in high-MA compositions are less clear from literature [25, 1, 20]. The extracted instability index results are thus further validated via pre- and post-aging XRD (shown in the Supplemental Information). The post-aging XRD peaks of hexagonal $FAPbI_3$ first increase with increasing MA proportion but start to decrease after more than 50% of MA is added, which matches the degradation observed via the computer vision approach. At the same time, the other possible major degradation route via perovskite decomposition [23] can be ruled out based on XRD. As a result, we link the color change to the transformation of cubic $FA_{1-x}MA_xPbI_3$ to a hexagonal crystal structure. The presence of the hexagonal $FAPbI_3$ phase indicates degradation from the more electrically favorable cubic $FAPbI_3$ phase [15].

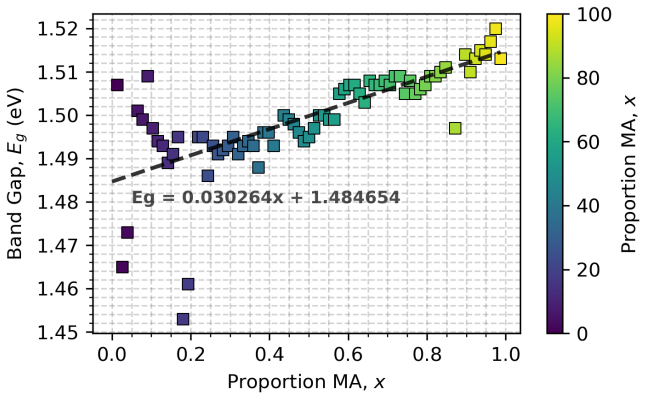

(a) Extracted Band Gaps

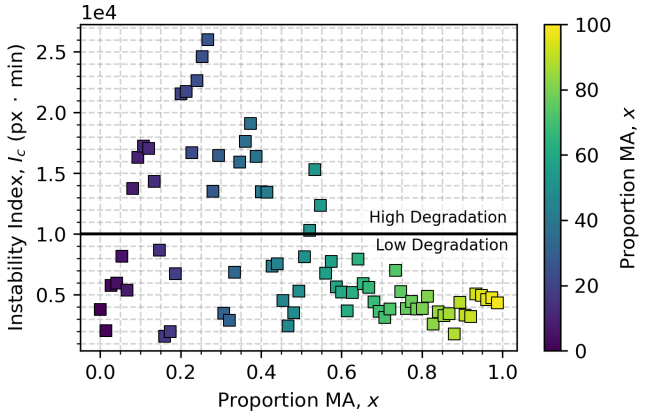

(b) Extracted Instability Index

Figure 6: The output (a) band gaps and (b) instability indices from the band gap and stability autocharacterization methods. Each uniquely segmented sample, Φ, is plotted as a colored square marker with its color and x-axis position corresponding to the proportion of MA in $FA_{1-x}MA_xPbI_3$. (a) The equation of the regression line fit to the $E_g(x)$ curve is displayed in the chart area. (b) The I_c is thresholded at a value of 10000 to indicate high degradation above the threshold and low or no degradation below.

To further validate the autocharacterization tools developed in this paper, we benchmark the extracted results with human-evaluated results. To measure the accuracy of each result, we take the difference between the set of human-evaluated reference results, $\mathbf{Z}_{\text{ref}}$, and the set of automatically extracted results, $\mathbf{Z}_{\text{ext}}$, and divide the difference by the total maximum difference:

$$\text{Acc.} = \left(1 - \frac{|\mathbf{Z}_{\text{ref}} - \mathbf{Z}_{\text{ext}}|}{\texttt{Max}(\mathbf{Z}_{\text{ref}}, \mathbf{Z}_{\text{ext}}) - \texttt{Min}(\mathbf{Z}_{\text{ref}}, \mathbf{Z}_{\text{ext}})}\right) \times 100 \tag{6}$$

For the band gap data, $\mathbf{Z}_{\text{ref}}$ is a set of numerical band gap

results in electronvolts (eV) acquired by a domain expert through manual regression line fitting of Tauc plots to Ω, who has not seen the set $\mathbf{Z}_{\text{ext}}$ computed from Φ. For the stability data, $\mathbf{Z}_{\text{ref}}$ is a binarized set acquired by a domain expert through manual regression line fitting of Tauc plots to the post-degradation Ω. If no band gap exists after degradation, this implies high degradation has occurred and a value of 1 is assigned, otherwise, a value of 0 is assigned. Similarly, for the stability data, $\mathbf{Z}_{\text{ext}}$ is a binarized set acquired by thresholding I_c at 10000 px $\cdot$ min, as shown in Figure 6(b), where $I_c > 10000$ implies high degradation has occurred and a value of 1 is assigned, otherwise, a value of 0 is assigned. Finally, for the composition data, no direct measure of composition was taken in this study, thus, $\mathbf{Z}_{\text{ref}}$ is inferred by computing x from the regression line fit of the extracted band gap data, as shown in Figure 6(a), and the error of the fit is propagated to the composition accuracy calculation.

Method	Accuracy (%)
Composition	78.77 ± 9.4
Band Gap	$\mathbf{89.08 \pm 7.3}$
Stability	87.84 ± 7.5

Table 1: Results of the vision-driven autocharacterization methods relative to a human evaluation reference. Accuracy is shown as a percentage with the 95% confidence interval shown in the error.

Table 1 shows the accuracy, computed using Equation 6, for each autocharacteriztion method developed in this paper. The automatic band gap extraction method demonstrates the highest accuracy of the three methods at 89.1%, relative to its human-evaluation counterpart. The simple linear relationship between x and E_g within the $FA_{1-x}MA_xPbI_3$ system supports the high performance of the automatic band gap extraction method. Conversely, the trace of $I_c(x)$ is parabolic rather the linear, like $E_g(x)$, implying that there are more complex chemical mechanisms at work during stability testing. We note the automatic stability measurement method has an accuracy of 87.8%, slightly lower than that of the automatic band gap extraction. Finally, the composition extraction process has an accuracy of 78.8%, which is significantly lower than the accuracies of the other autocharacterization methods, due to error propagation in acquiring $\mathbf{Z}_{\text{ref}}$ for composition in this study. Overall, each of the three autocharacterization methods developed in this paper exhibits high accuracy between 78%–89%, compared to human evaluation. Furthermore, the key contribution of the developed autocharacterization methods extends past simply accelerating the throughput of sample-by-sample characterization and more largely drives scalable characterization of arbitrarily many samples through the use of computer vision, such that characterization is no longer the bottleneck process in high-throughput materials screening.

4. Conclusions

In the modern-day exploration of novel materials, synthesis is no longer the bottleneck process due to the paradigm shift towards autonomous and self-driving laboratories [14, 10, 6, 19]. For example, in this paper, we synthesize 80 unique perovskite semiconductor materials along the $FA_{1-x}MA_xPbI_3$ sequence in only 16.5 seconds. Instead, the bottleneck for novel material discovery is now the manual characterization of each sample individually [22]. Although strides have been made with some autocharacterization methods of materials, there is a lack of scalability to these methods to arbitrarily many samples, as produced by high-throughput synthesis hardware, thus, inhibiting the throughput of materials discovery [21]. Integration of computer vision in tandem with autocharacterization has the promise of improving this throughput. However, conventional computer vision approaches for materials-specific tasks have been used predominately for morphological analyses in combination with specialized microscopy methods [18, 3]. In this paper, we proposed the design of three autocharacterization tools to compute (i) composition, (ii) band gap, and (iii) stability of perovskite semiconductors and integrate each of these tools with computer vision segmentation of optical reflectance data to further automate and accelerate the characterization pipeline.

Through the use of high-fidelity computer vision segmentation, we demonstrate the scalability of accurate and automatic characterization for 80 unique $FA_{1-x}MA_xPbI_3$ perovskite samples. The developed vision segmentation method avoids edge effects and removes aberrations to output a clean segmentation of optical data. From the segmented optical data, the automatic band gap computation is demonstrated to achieve an accuracy of 89.1%, the automatic stability measurement is demonstrated to achieve an accuracy of 87.8%, and the automatic composition extraction is demonstrated to achieve an accuracy of 78.8% across all 80 perovskite samples, relative to a human evaluation reference. Furthermore, the results extracted by the developed vision-driven autocharacterization tools are validated to align with traditional x-ray diffraction characterization. The results achieved by the methods developed in this paper support the advancement of scalable, high-throughput novel materials discovery by surmounting the obstacle of sample-by-sample characterization.

References

[1] Bethan Charles, Jessica Dillon, Oliver J. Weber, M. Saiful Islam, and Mark T. Weller. Understanding the stability of mixed a-cation lead iodide perovskites. *Journal of Materials Chemistry A*, 5:22495–22499, 11 2017. 7

[2] Hua Chen and Lawrence B. Wolff. *International Journal of Computer Vision*, 28(1):73–83, 1998. 2

[3] Aritra Chowdhury, Elizabeth Kautz, Bülent Yener, and Daniel Lewis. Image driven machine learning methods for microstructure recognition. *Computational Materials Science*, 123:176–187, 2016. 2, 8

[4] A. Escobedo-Morales, I. I. Ruiz-López, M. de L. Ruiz-Peralta, L. Tepech-Carrillo, M. Sánchez-Cantú, and J. E. Moreno-Orea. Automated method for the determination of the band gap energy of pure and mixed powder samples using diffuse reflectance spectroscopy. *Heliyon*, 5:e01505, 4 2019. 2

[5] Vivien Sainte Fare Garnot and Loic Landrieu. Panoptic segmentation of satellite image time series with convolutional temporal attention networks. In *Proceedings of the IEEE/CVF International Conference on Computer Vision*, pages 4872–4881, 2021. 1

[6] Kedar Hippalgaonkar, Qianxiao Li, Xiaonan Wang, John W. Fisher, James Kirkpatrick, and Tonio Buonassisi. Knowledge-integrated machine learning for materials: lessons from gameplaying and robotics. *Nature Reviews Materials 2023*, pages 1–20, 1 2023. 1, 8

[7] Rodolfo Keesey, Armi Tiihonen, Alexander E Siemenn, Thomas W Colburn, Shijing Sun, Noor Titan, Putri Hartono, James Serdy, Margaret Zeile, Keqing He, Cole A Gurtner, Austin C Flick, Clio Batali, Alex Encinas, Richa R Naik, Zhe Liu, Felipe Oviedo, I Marius Peters, Janak Thapa, Siyu Isaac, Parker Tian, Reinhold H Dauskardt, Alexander J Norquist, and Tonio Buonassisi. An open-source environmental chamber for materials-stability testing using an optical proxy. *Digital Discovery*, 2023. 2, 4, 6, S-3

[8] Thomas Leung and Jitendra Malik. *International Journal of Computer Vision*, 43(1):29–44, 2001. 2

[9] Hanjun Li, Xingjia Pan, Ke Yan, Fan Tang, and Wei-Shi Zheng. Siod: Single instance annotated per category per image for object detection. In *Proceedings of the IEEE/CVF Conference on Computer Vision and Pattern Recognition (CVPR)*, pages 14197–14206, June 2022. 1, 2

[10] Benjamin P. MacLeod, Fraser G.L. Parlane, Connor C. Rupnow, Kevan E. Dettelbach, Michael S. Elliott, Thomas D. Morrissey, Ted H. Haley, Oleksii Proskurin, Michael B. Rooney, Nina Taherimakhsousi, David J. Dvorak, Hsi N. Chiu, Christopher E.B. Waizenegger, Karry Ocean, Mehrdad Mokhtari, and Curtis P. Berlinguette. A self-driving laboratory advances the pareto front for material properties. *Nature Communications 2022 13:1*, 13:1–10, 2 2022. 1, 8

[11] Patrycja Makuła, Michał Pacia, and Wojciech Macyk. How to correctly determine the band gap energy of modified semiconductor photocatalysts based on uv-vis spectra. *Journal of Physical Chemistry Letters*, 9:6814–6817, 12 2018. 5

[12] Paolo Menesatti, Claudio Angelini, Federico Pallottino, Francesca Antonucci, Jacopo Aguzzi, and Corrado Costa. Rgb color calibration for quantitative image analysis: The "3d thin-plate spline" warping approach. *Sensors*, 12(6):7063–7079, 2012. 6

[13] Fernand Meyer. Topographic distance and watershed lines. *Signal Processing*, 38:113–125, 7 1994. 4

[14] Shahram Moradi, Soumya Kundu, Milad Rezazadeh, Vishal Yeddu, Oleksandr Voznyy, and Makhsud I. Saidaminov. High-throughput exploration of halide perovskite compositionally-graded films and degradation mechanisms. *Communications Materials 2022 3:1*, 3:1–5, 3 2022. 1, 8

[15] Zeeshan Muhammad, Peitao Liu, Rashid Ahmad, Saeid Jalali-Asadabadi, Cesare Franchini, and Iftikhar Ahmad. Revealing the quasiparticle electronic and excitonic nature in cubic, tetragonal, and hexagonal phases of fapbi3. *AIP Advances*, 12:025330, 2 2022. 7

[16] Reyhaneh Neshatavar, Mohsen Yavartanoo, Sanghyun Son, and Kyoung Mu Lee. Cvf-sid: Cyclic multi-variate function for self-supervised image denoising by disentangling noise from image. In *Proceedings of the IEEE/CVF Conference on Computer Vision and Pattern Recognition (CVPR)*, pages 17583–17591, June 2022. 2

[17] Chiwoo Park and Yu Ding. Automating material image analysis for material discovery. *MRS Communications*, 9(2):545–555, 2019. 1, 2

[18] Chiwoo Park, Jianhua Z. Huang, David Huitink, Subrata Kundu, Bani K. Mallick, Hong Liang, and Yu Ding. A multistage, semi-automated procedure for analyzing the morphology of nanoparticles. *IIE Transactions*, 44(7):507–522, 2012. 2, 8

[19] Edward O. Pyzer-Knapp, Jed W. Pitera, Peter W. Staar, Seiji Takeda, Teodoro Laino, Daniel P. Sanders, James Sexton, John R. Smith, and Alessandro Curioni. Accelerating materials discovery using artificial intelligence, high performance computing and robotics. *npj Computational Materials*, 8(1), 2022. 1, 8

[20] Laura T. Schelhas, Zhen Li, Jeffrey A. Christians, Anuj Goyal, Paul Kairys, Steven P. Harvey, Dong Hoe Kim, Kevin H. Stone, Joseph M. Luther, Kai Zhu, Vladan Stevanovic, and Joseph J. Berry. Insights into operational stability and processing of halide perovskite active layers. *Energy Environmental Science*, 12:1341–1348, 4 2019. 7

[21] Alexander E. Siemenn, Evyatar Shaulsky, Matthew Beveridge, Tonio Buonassisi, Sara M. Hashmi, and Iddo Drori. A machine learning and computer vision approach to rapidly optimize multiscale droplet generation. *ACS Applied Materials Interfaces*, 14:4668–4679, 1 2022. 1, 3, 8

[22] Shijing Sun, Noor T.P. Hartono, Zekun D. Ren, Felipe Oviedo, Antonio M. Buscemi, Mariya Layurova, De Xin Chen, Tofunmi Ogunfunmi, Janak Thapa, Savitha Ramasamy, Charles Settens, Brian L. DeCost, Aaron G. Kusne, Zhe Liu, Siyu I.P. Tian, Ian Marius Peters, Juan Pablo Correa-Baena, and Tonio Buonassisi. Accelerated development of perovskite-inspired materials via high-throughput synthesis and machine-learning diagnosis. *Joule*, 3:1437–1451, 6 2019. 1, 5, 7, 8

[23] Shijing Sun, Armi Tiihonen, Felipe Oviedo, Zhe Liu, Janak Thapa, Yicheng Zhao, Noor Titan Hartono, Anuj Goyal, Thomas Heumueller, Clio Batali, and et al. A data fusion approach to optimize compositional stability of halide perovskites. *Matter*, 4(4):1305–1322, 2021. 1, 4, 6, 7, S-3

[24] Zejin Wang, Jiazheng Liu, Guoqing Li, and Hua Han. Blind2unblind: Self-supervised image denoising with visi-

ble blind spots. In *Proceedings of the IEEE/CVF Conference on Computer Vision and Pattern Recognition (CVPR)*, pages 2027–2036, June 2022. 2

[25] O. J. Weber, B. Charles, and M. T. Weller. Phase behaviour and composition in the formamidinium–methylammonium hybrid lead iodide perovskite solid solution. *Journal of Materials Chemistry A*, 4:15375–15382, 10 2016. 7